FLYWHEEL: JURNAL TEKNIK MESIN UNTIRTA

Homepagejurnal: http://jurnal.untirta.ac.id/index.php/jwl

Investigation of The Decay of a Single vortex with PIV Technique

Surjo Abadi

Program Studi Teknik Mesin, Universitas Kristen Indonesia, Jl. Mayjen Sutoyo Cawang no 2 Jakarta 13630, Indonesia
suryo.abadi@uki.ac.id

ARTICLE INFO

Received 5/9/2020
revision 12/11/2020
accepted 20/11/2020
Available online 23/11/2020

ABSTRACT

The formation and development of a single vortex are investigated in a wind tunnel. The wake from a rectangular lifting wing based on a CLARK-Y profile of 11.7% is studied up to 80 chords downstream. Digital particle image velocimetry is used to measure the velocity field in the cross-stream plane from which is the vortex is measured. Two different experimental tests were carried out in two different tunnel conditions, without and with a grid. From the first condition, the vortex is observed to be relatively stable and long–lived. A correlation for the peak tangential velocity u_θ, max, and the vortex core r_c has been compared with the Lamb-Oseen model, and it gives a fair agreement. The circulation Γ is observed to be proportional to the free-stream U_∞ (range 8 – 20 m/s) and the angle of attack α (range 1–12 deg). The vorticity ω, however, diffuses over time within the growth of the vortex core r_c. The Squire model can approach this growth. The vortex characteristics become weaker when the experiments are performed under grid turbulence conditions. Due to the influence of the grid turbulence, some experiments give inconsistent results. It is made it difficult to conclude. However, still, some interesting information is found in this case.

Keywords: *fluid mechanic, vortex, PIV Technique, Wingtip*

1. INTRODUCTION

The wake vortices generated by an aircraft wing have been a subject of interest in this research. It has been well known that when an aircraft takes off, its wing generates not only the required lift force but also produces horizontal tornado-like vortices called *Wake Vortices* or *Trailing Vortices*, see Figure 1[1,2].

These vortices are long-lived, mostly invisible, difficult to predict, and a severe threat to the following aircraft, especially during taking-off and landing phases. Studies have shown that the vortex's strength is directly proportional to the weight, the wingspan, and the speed of the aircraft. A heavy aircraft generates more robust circulation than a smaller aircraft. Flight tests [3] pointed out that a small aviation aircraft can create vortices that are almost undetectable by trailing aircraft of similar size. However, large jetliners leave vortices that can exceed 240 km/h in rotational velocity, and they are still detectable at distances of 32 km behind the aircraft[4,5].

Figure 1. Wing-tip vortex visualized by smoke.

Since trailing vortices tend to persist for long distances downstream, they form a potential hazard for the following aircraft. For safety reasons, a minimum spacing during the aircraft landing and taking-off are

required to avoid the wake vortex encounter. These spacing standards restrict the capacity of many airports and thus negatively impacting the airline industry. The demand for increased air traffic has led to enormous passenger aircraft construction with a more robust wake. Nowadays, it is challenging to develop additional airport capacity due to economic and environmental reasons[6–9].

The effect of the ambient turbulence on the vortex instability has been observed by Liu [10,11]. His investigation was conducted in a towing tank, measured 18 m long, 1.2 m wide, and 0.9 m deep. The trailing vortices were generated by towing a rectangular wing with a span of 5.1 cm and a chord of 2.5 cm. Liu has shown that the vortex aging is proportional to the turbulence's intensity in the mean flow, see Figure 2.

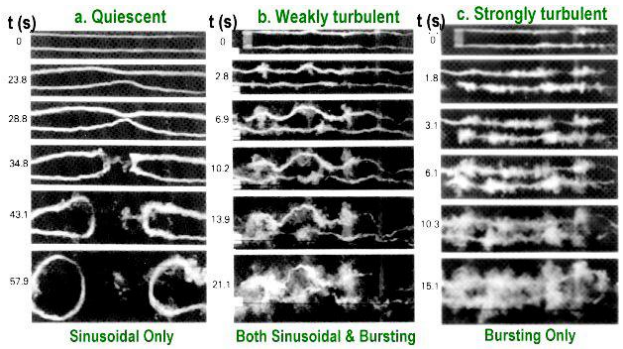

Figure 2. The effect of ambient turbulence on the vortex instability, Liu [10].

Figure 2 shows that the destruction of the trailing vortices in the absence of ambient turbulence (on the left column) takes much more time than in healthy turbulent conditions (on the right column). In the absence of external turbulence, a sinusoidal movement at the vortices is the only form of instability. This leads to the reconnection of the vortex lines (the so-called Crow instability [2]). While in the weak turbulent condition (on the middle column), both sinusoidal and bursting instabilities are found. In the healthy turbulent condition (on the right column), the vortices instability is predominantly the bursting type. The observation reveals that the external turbulence can accelerate the decay process of the vortex pairs[12].

The Fluid Dynamics Laboratory of TU/e (Eindhoven University of Technology) participates in the EU FARWAKE program, which studies the fundamental aspect of aircraft trailing vortices[13,14]. This research's vital objective is to improve the physical understanding of wake-vortex evolution and decay in the atmosphere. This research's activities described in this report will be focused on: the formation and development of a single vortex, including the effects of varying the central stream velocity and the decaying of a vortex influenced by external turbulence.

The PIV (Particle Imaging Velocimetry) technique is used in this observation[15,16]. This technique involves introducing a mist of fine particles, such as droplets of olive oil, into the air stream. A laser creates a sheet of light downstream of the model aircraft and, as the particles pass through the sheet, they are photographed by a high-speed camera. Consequently, the PIV technique always results in a significant number of images that must be further processed[17–19].

2. EXPERIMENTAL SET-UP AND MEASUREMENT TECHNIQUE

2.1 *Experimental apparatus*

All experiments were performed in the closed-circuit wind tunnel in the Fluid Dynamics Laboratory. The wind tunnel is a closed return, closed test section wind tunnel for medium speeds with test section dimensions of 8 m long, 0.7 m wide, and 1.05 m height. This wind tunnel is depicted in Figure 3.

Both sides of the test section consist of easily removable plexiglass slide plates. It allows convenient optical access to the tunnel[15,8]. The tunnel is driven by a fan coupled to the shaft of a variable speed motor. The rotation speed of the motor can be varied from 0 to 560 rpm. The maximum wind speed in the tunnel that can be reached is 20 m/s. This tunnel can be utilized with a so-called 'active grid,' a turbulence grid that can be activated with electromotors to generate turbulence with specific characteristics. The essential grid was made of 1 cm diameter rods with a 10 cm mesh distance. In the present experiment, the grid was either removed or used in its passive mode.

Figure 3. The wind tunnel.

A specifically designed single-airfoil is used as a vortex generator in the experiments, as illustrated in Figure 4. This vortex generator consists of a rectangular half-wing with span b of 0.35 m, chord length c of 0.075 m with a CLARK-Y airfoil section of 11.7 % thick, and an increasing wing twist from root till the tip. The angle of attack α, and the span b of the wing, can be adjusted from outside the tunnel. This wing is fixed at the sidewall of the tunnel. In the middle of the wing, a small hole is made such that tracer particles (e.g., smoke) can be injected near the wing-tip[20].

2.2 Reference system

The Cartesian coordinate system's origin is located at the tip of the vortex generator (Fig. 5). The origin **O**(*x, y, z*) coincides with the vortex generator's trailing edge.

The *x*-axis is parallel to the wind tunnel axis, positive in the downstream direction. The *z*-axis axis is vertical, upward oriented. The *y*-axis is horizontal oriented perpendicular to the wall of the tunnel.

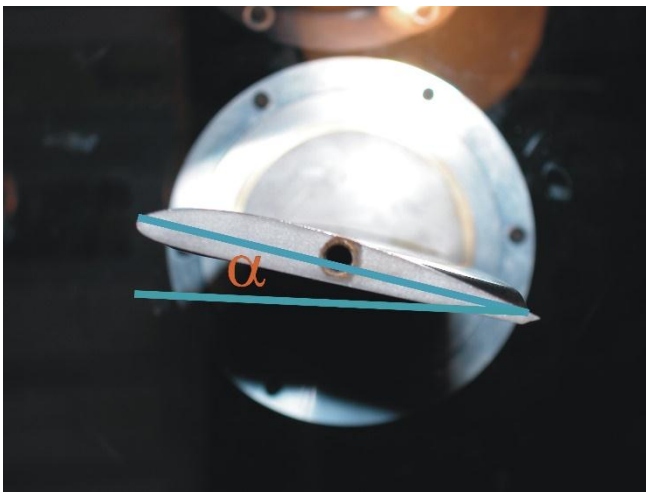

Figure 4. Wing model Clark-Y 11.7%.

2.3 Experimental set-up

The outline of the experimental set-up is schematically displayed in Figure 6. The airflow enters the test section of the wind tunnel with velocity U_∞. The speed of the airflow in the tunnel can be adjusted by controlling the motor's rotation speed. To visualization the wake vortex, trace particles are injected into the main flow at two different places.

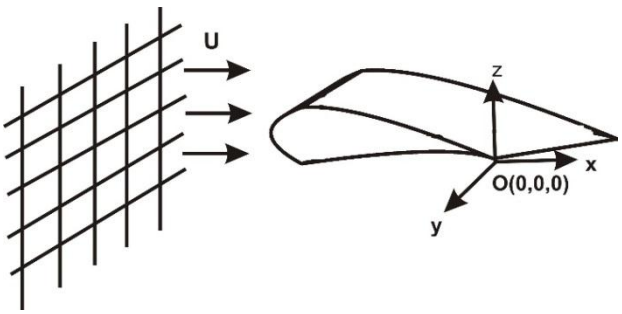

Figure 5. Reference coordinate system.

The first is a small opening place in the near wing-tip (Fig. 4), and the second is at the rear of the test section place from the ceiling of the tunnel. The particles, suspended in the airflow, flow through the vertical measurement plane. At the measuring plane's position, these particles are illuminated by a thin laser light sheet twice within a short time interval, Δt. The time interval must be sufficiently small so that the particles seen in the first image are still present in the second image. The light scattered by the tracer particles is then recorded by a CCD camera placed behind the laser sheet. Various downstream positions behind the vortex generator have been investigated.

Two sets of experiments have been made. The first set focused on the formation of the wake vortex as a function of the tunnel speed. These tests aimed to determine the model characteristics and hence the vortex's starting condition as a function of the tunnel speed. The second set of experiments paid attention to the decaying vortex.

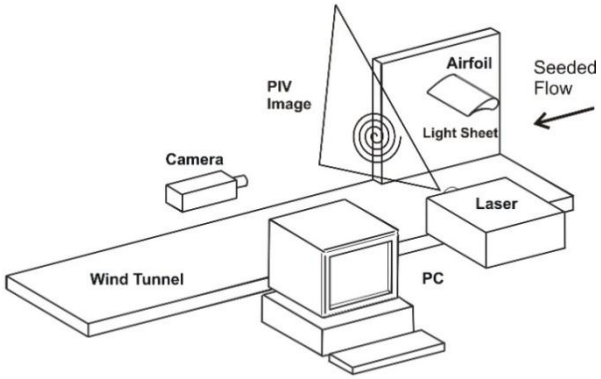

Figure 6. Schematic representation of the experimental set-up.

To observe the phenomenon, the wake vortex was measured at a different position in the downstream direction. Both sets of the experiments were conducted under two conditions of the tunnel, i.e., with external turbulence and without external turbulence. The turbulence grid was added in front of the test section To achieve the turbulence in the tunnel[21].

2.3.1 Measurement system

As mentioned above, the tracer particles' movements are monitored by a CCD camera in a plane perpendicular to the cross-section of the tunnel (see Fig. 5). The recorded image quality is an essential factor for the PIV technique to determine the velocity fields in the vortex. The image of a recorded image pair is divided into small sub-areas called "interrogation area" IA, which have typical dimensions of, for instance, 16 × 16, 32 × 32, or 64 × 64 pixels^2. The' mean' local displacement of the particle images in the interrogation area between the first image and the second image is determined utilizing a cross-correlation function. Furthermore, the local average velocity in the laser light sheet plane can be determined by dividing the displacement vector (using an appropriate scaling factor) through the time interval Δt between the first and the second image. This procedure is repeated for all defined interrogation areas. To estimate the velocity fields in the entire recorded area[12,16].

During the experiment, the in-house software has been used to determine the velocity vector fields and the cross-correlation between the interrogation areas and the corresponding physical areas. This software allows the user to choose the size of the interrogation area[22]. The velocity fields acquired from this software are saved in a four columns matrix that contains each position (y, z) of the velocity vectors (u_y, u_z). An investigation by employing the PIV technique usually results in many images that must be further processed. Numerous routines have been developed using MATLAB.

2.3.2 Measurements instrumentation

A double pulsed Nd.YAG (Neodymium Yttrium Aluminum Garnet) laser type CFR 200 Big Sky Laser was used as the light source. The laser emits light with a wavelength of 532 nm. One laser pulse has a duration of 6 ns and maximum energy of 200 mJ/pulse.

Next, the images captured at the laser sheet are recorded by a CCD camera, Kodak Megaplus 10-bit ES 1.0 1008 × 1019 pixels2. This camera records images at a maximum frame rate of 29 Hz. Different Nikon lenses (f 10, f 12, f 28) were used in front of the CCD camera. The camera was positioned at a certain distance behind the laser sheet mounted in the wind tunnel. During the observation, the camera is set in the triggering mode, meaning that the image frames are captured at each triggering pulse coming from an external pulse generator. By activating the double exposure mode, it is possible to record two images in a short period. This short period corresponds with the time interval set to 20 µs and 50 µs. A delay generator was used to control the camera's delay and integration period concerning the laser pulse. In each case, approximately 500 images were recorded. This number corresponds to 250 images pair from which the displacement or velocity fields are calculated.

The wake-vortex was made visible by releasing fine particles into the tunnel. The flow in the tunnel is seeded by DEHS (di-2-ethyl hexyl sebacate) tracer particles. Two particle generators are used at the same time during the measurements. Aerosol Generator AGF 2.0 injects particles at the wing-tip directly in the vortex center. The DNW (Deutsch Nederland Windtunnel) Aerosol Generator injects particles at the rear of the test section. The particles from both generators then mix and circulate together with the wind in the tunnel. The purpose of injecting particles at a different place at the same time during the experiments is to have a high seeding density.

3. DATA PROCESSING

Using the PIV technique usually results in many images and data that must be further processed. The post-processing technique is an essential factor in analyzing the data of the experiment. The subsequent steps of the post-processing are schematically depicted in Figure 7.

After the automatic evaluation of the PIV recording, the velocity fields' information is saved in a four columns matrix, which contains the position of the velocity vector (y, z) and the magnitude of the vector (u_y, u_z).

This matrix forms the start of the subsequent post-processing (Figure 7). In the raw data, a certain number of incorrect vectors can usually be found by visual inspection, the so-called outliers. In order to detect these incorrect vectors, the raw data needs to be validated. For this purpose, a special algorithm is developed.

The second step of the post-processing is extraction of the parameters of the vortex, to be used to describe and analysis the behaviour of the vortex. The important parameters that needs to be determined are: the vorticity, the circulation, the maximum tangential velocity, and the vortex radius. Typically the PIV technique results in several thousands of data points per picture. It is difficult to work with several thousand velocity vectors and to describe their fluid mechanical features. Therefore some kind of averaging is applied in this experiment to reduce the PIV data.

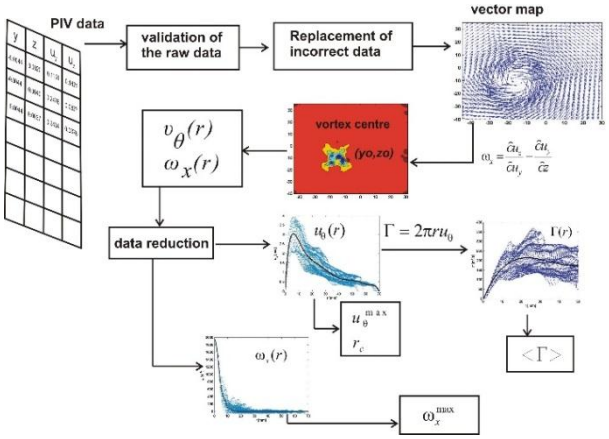

Figure 7. Schematic representation of the post processing of PIV data.

3.1 Data validation

A significant problem associated with PIV raw data after evaluating PIV images can be seen in Figure 8. It shows the vectors field at a position 0.15 m behind the wing where the free stream velocity U_∞ is 14 [m/s]. By visual observation, the outliers can be easily recognized as mismatches in the observed pattern.

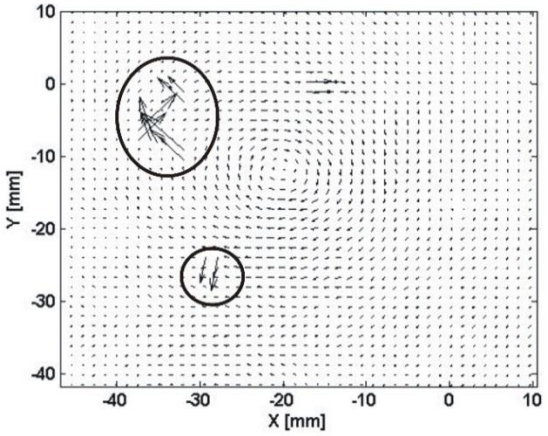

Figure 8. The velocity vector map of the vortex behind the wing. The outliers are marked by circles.

The experiment revealed that the number of outliers strongly depends on the size of the interrogation area. Some of the PIV data are processed three times with different sizes of the interrogation area, viz 16 × 16, 32 × 32, and 64 × 64 pixels^2 to see the effect of different interrogation area sizes the number of outliers. Using the program developed by Westerweel [23], the number of outliers in the PIV data can be determined, as shown in Table 1. Table 1 shows that the number of outliers in the 64 × 64 window is smaller compared to the other

cases. In this study, it was decided to use a window of 64 × 64 pixels for the processing of the PIV data.U∞ is 14 [m/s].

Tabel 1. Number of outliers for different sizes of the interrogation area where $\boldsymbol{U}_{\infty}$ = 11 m/s.

$\Delta x \times \Delta y$ (pixel)	Number of vector	Outliers (%) $U_\infty = 11\ m/s$
16 × 16	31500	22,6
32 × 32	7688	17,6
64 × 64	1800	8

3.2 Outlier filtering

The vector maps are validated using a median filter To remove the incorrect vectors from the experimental data. This filter has been proposed by Westerweel [23]. This nonlinear filter is frequently utilized in image processing to remove the binary noise. The median filter's effect is demonstrated in Figure 9, where all erroneous velocity data have been deleted, and velocity vectors are identified, having magnitude and direction.

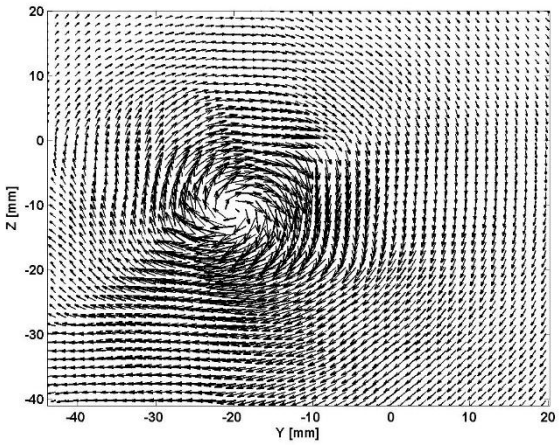

Figure 9. The velocity vector map of the vortex after clean-up.

3.3 Determining vortex parameters

After having improved the PIV data and having smoothed and interpolated the data on a regular grid, the PIV data's velocity fields can be used to determine the axial vorticity field ωx by taking the curl of the velocity field.

$$\boldsymbol{\omega_x} = (\boldsymbol{\nabla} \times \boldsymbol{u}) = \frac{\boldsymbol{\delta u_z}}{\boldsymbol{\delta y}} - \frac{\boldsymbol{\delta u_y}}{\boldsymbol{\delta z}} \qquad (1)$$

In equation (1), u_y and u_z represent the velocity components in the y and z-direction. Figure 10 represents the result of the axial vorticity field together with the velocity field. From this figure, it can be noticed that the center location of the vortex roughly corresponds to the peak value of the vorticity.

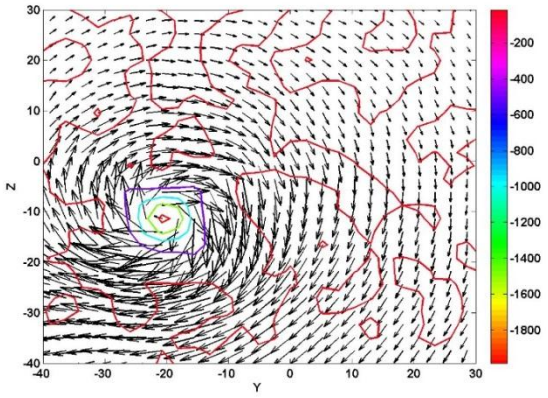

Figure 10. The velocity vectors (marked by small black arrows), and the axial vorticy (denoted by contours).

This indication is used to determine the location of the vortex center (y_o, z_o). After determining the vortex's center location, the cartesian coordinate system is transformed into a polar coordinate system so that all parameters of the vortex can be represented as a function of the radius r. If it is assumed that the velocity in y and z-direction is roughly perpendicular to the vortex radius; the tangential velocity u_θ of the vortex is then given by :

$$\boldsymbol{u_\theta} \cong \sqrt{\boldsymbol{u_y^2} + \boldsymbol{u_z^2}} \qquad (2)$$

An averaged smoothing (Moving Average) method is then applied to obtain the tangential velocity has smoothed value, u_θ as a function of the radius r, see Figure 11. From this figure, the circulation Γ over a closed area A can be obtained by integration of the tangential velocity u_θ along the outer contour C. Assuming that the contour of C is a circle, then the equation of the circulation is given:

$$\boldsymbol{\Gamma(r)} = \int_0^{2\pi} \boldsymbol{u_\theta}\,(\boldsymbol{r}, \boldsymbol{\theta}) \boldsymbol{r d\theta}, \qquad (3)$$

With r is the radius of the circle. For a single vortex, the value of the circulation is nearly constant for $r \to \infty$.

In this study, the circulation value is approximating by taking an average value of $< \Gamma(r) >$ away from the vortex center,

$$< \boldsymbol{\Gamma} > = \frac{1}{\boldsymbol{r_2 - r_1}} \int_{r1}^{r2} \int_0^{2\pi} \boldsymbol{r u_\theta(r, \theta) dr d\theta} \qquad (4)$$

The value of r_1 and r_2 are selected based on an inspection of the graph. A smoothing average is also applied to the circulation, see Figure 12. From the figure, it can be seen that a solid line indicates the result of the smoothed average. The circulation's average value is

calculated over circles with a range from radius r_1 to radius r_2.

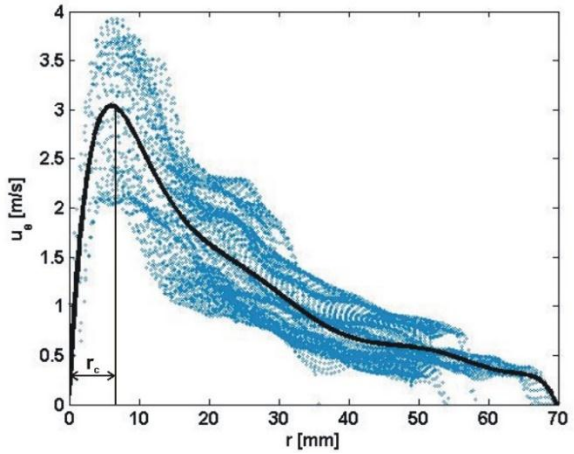

Figure 11. Obtaining the tangential velocity profile with smoothing average method.

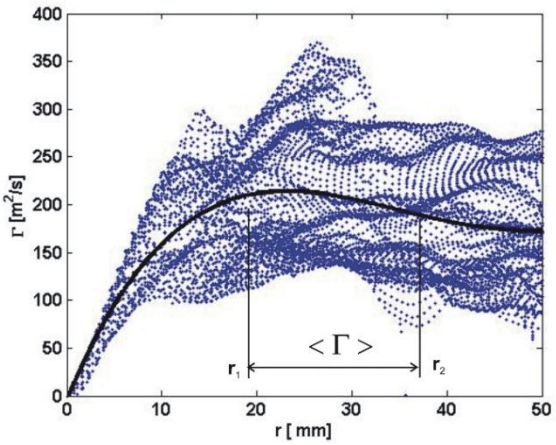

Figure 12. Obtaining circulation with smoothing average method.

4. RESULTS

4.1 The tangential velocity

The tangential or cross-wise velocity is the velocity component in the cross-flow plane perpendicular to the vortex axis. Typical velocity profiles for a single vortex are shown in Figure 13. The figure represents the averaged velocity profile based on 100 images of PIV data at four different downstream stations. The velocity profiles are presented in a non-dimensional way $\boldsymbol{u_\theta/U_\infty}$ versus *r/c*, where $\boldsymbol{u_\theta}$ represents the azimuthal or tangential velocity, $\boldsymbol{U_\infty}$ is the main stream velocity, *r* represents radial distance to the centre of the vortex and c is the wing chord length. The various stations are plotted in one figure. The distance of the station behind the tip of the wing are: station one: x_1 = 0.15 m, station two: x_2 = 1.0 m, station three: x_3 = 3.5 m, and station four: x_4 = 5.35 m.

In the figure, a comparison is made with the velocity as defined by a line vortex for a range of assumed non-dimensional vortex strength values ($\boldsymbol{\Gamma/(U_\infty c)}$), where is the circulation.

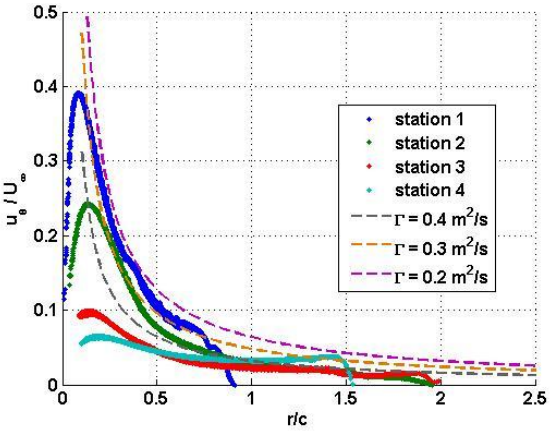

Figure 13. The radial distribution of the tangential velocity for every station. Note that the experiments were carried out for a tunnel speed 11.33 m/s, without grid, and the angles of attack α =7.5 deg.

In the figure, one can see that the velocity increases with increasing radius *r* until a maximum value is reached at the core radius around *r/c* = 0.1 or 0.2. At larger values for *r* , all the curves should ideally approach a line vortex's velocity distribution.

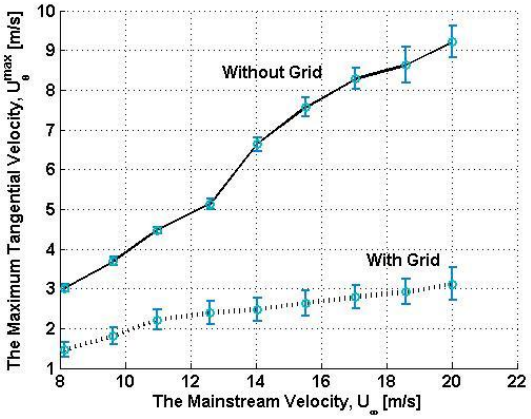

Figure 14. The maximum tangential velocity as a function of the tunnel speed $\boldsymbol{U_\infty}$ with and without grid turbulence. The recording was carried out at *x* = 0.15 m behind the wing and an attack the angles α =7.5 deg.

From the figure, it can be seen that this is not the case, and the results look inconsistent. The first station's velocity profile is very close to the line of non-dimensional circulation ($\boldsymbol{\Gamma}$= 0.4), but this is not followed by the velocity profile measured at the second station. There is an apparent difference in circulation between the first station and the second station. These differences have become more extensive when we consider the velocity profiles in stations three and four.

The azimuthal velocity profile has a maximum value at distance r_c from its center. This peak value, max, is influenced by the central stream velocity, see Figure 14.

The experiments were repeated with a turbulence grid in the tunnel to see the vortex behavior under turbulence conditions. A comparison between the result of experiments with and without grid can also be seen in Figure 14. The peak value of the tangential velocity profile with a grid is much lower than without a grid.

4.2 Circulation

The observations show that the circulation decreases from one station to the other station. The circulation values at station four are compared to station one's circulation values better to understand the apparent decay in the stream-wise direction; the circulation values at station four are compared to station one's circulation values.

The experiment is also set up where the grid is installed in the tunnel. Tables 2 and 3 show the decaying circulation in percentage and the downstream for each tunnel speed give almost the same result, i.e., around 60 %. This dissipation is quite large; more than half of the vortex strength vanishes.

Table 2. The decaying of circulation $\boldsymbol{\Gamma}$ along the tunnel for each tunnel speed, and without grid condition.

U_∞ [m/s]	$\Gamma_o[m^2/s]$	$\Gamma_4\ [m^2/s]$	Γ_4/Γ_o
8.16	0.19	0.09	0.52
9.75	0.23	0.24	1.01
11.33	0.29	0.16	0.55
12.91	0.35	0.19	0.56
14.39	0.46	0.23	0.51
15.93	0.52	0.28	0.54
17.48	0.57	0.34	0.59
19.00	0.62	0.38	0.61
20.47	0.67	0.43	0.64
$< \Gamma_4/\Gamma_o >$			$\approx 61\%$

4.3 Vortex model

4.3.1 The Lamb-Oseen vortex model

The following relation describes the tangential velocity:

$$\boldsymbol{u_\theta} = \frac{\boldsymbol{\Gamma}}{2\pi r}\left[1 - \exp\left(1 - \boldsymbol{\beta}\left(\frac{r}{rc}\right)^2\right)\right] \quad (5)$$

where β = 1.256431 and Γ is the total circulation strength constant for infinite integration area. The vorticity distribution is given by:

$$\boldsymbol{\omega(r)} = \frac{\boldsymbol{\Gamma}}{\pi r_c^2}\boldsymbol{\beta}\ \exp[-\boldsymbol{\beta}(\frac{r}{r_c})^2] \quad (6)$$

4.3.2 The Burnham-Hallock vortex model

The velocity and the vorticity profiles of the Burnham-Hallock model are defined as :

$$\boldsymbol{u_\theta} = \frac{\boldsymbol{\Gamma}}{2\pi r}\frac{r^2}{(r_c^2+r^2)} \quad (7)$$

$$\boldsymbol{\omega(r)} = \frac{\boldsymbol{\Gamma}}{\pi r_c^2}\frac{1}{1+(r/r_c)^2} \quad (8)$$

Table 3. The decaying of circulation Γ along the tunnel for each tunnel speed, and with grid condition.

U_∞ [m/s]	$\Gamma_o[m^2/s]$	$\Gamma_4\ [m^2/s]$	Γ_4/Γ_o
7.57	0.13	0.09	0.69
8.96	0.17	0.11	0.63
10.35	0.22	0.13	0.58
11.77	0.27	0.15	0.56
13.21	0.30	0.17	0.57
14.68	0.34	0.18	0.55
16.13	0.36	0.21	0.58
17.57	0.37	0.21	0.55
19.00	0.39	0.22	0.56
$< \Gamma_4/\Gamma_o >$			$\approx 58\%$

4.3.3 The Winckelmans vortex model

The velocity and the vorticity profiles of the Winckelmans model are defined as :

$$\boldsymbol{u_\theta(r)} = \frac{\boldsymbol{\Gamma}}{2\pi r}\frac{r^2(r^2+2\gamma r_c^2)}{(\gamma r_c^2+r^2)^2} \quad (9)$$

$$\boldsymbol{\omega(r)} = \frac{\boldsymbol{\Gamma}}{\pi r_c^2}\frac{2\gamma^2}{(\frac{r}{r_c}+\gamma)^3} \quad (10)$$

where γ is 1.7808.

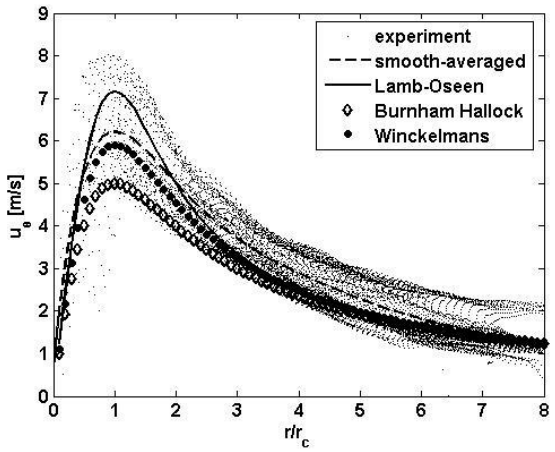

Figure 15. A comparison between experimental data and analytical models for velocity**.** Experimental conditions: the mainstream velocity in the tunnel is 14 m/s, the laser sheet is 0.15 m behind the wing-tip, in absence of grid.

When the measured circulation, $< \boldsymbol{\Gamma} >$ and the core radius, r_c, is substituted back into the vortex models, equations (5), (7), (9) the Lamb-Oseen, Burnham-Hallock, and Winkcelmans velocity distributions will be produced.

Figure 15 shows a comparison of the velocity profiles for the three vortex models. The figure shows that for equal vortex circulation strength and equal core radius, the peak velocity is the lowest for the Burnham-Hallock model and the largest for the Lamb-Oseen model. The Winckelmans model shows the closest agreement with the measured averaged smooth velocity profile.

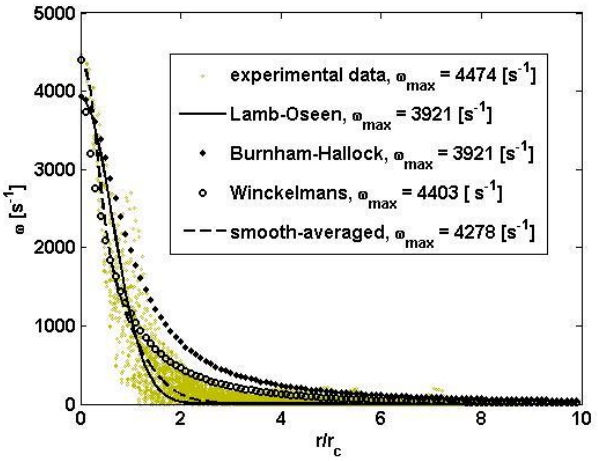

Figure 16. A comparison between experimental data and analytical models for vorticity. Experimental conditions: the mainstream velocity in the tunnel is 14 m/s, the laser sheet is 0.15 m behind the wing-tip, in absence of grid.

One can also make a comparison for the vorticity profile. By substituting equations; Eq. (6), (8), and (10), the vorticity profile of each model can be found, see Figure 16. The comparison shows a good agreement between the experimental data (marked by a dot), smooth averaged, and the Lamb-Oseen and Winckelmans model. Their maximum axial vorticities are close to each other. The Burnham-Hallock shows an enormous difference compared to the measured smooth averaged data.

5. CONCLUSIONS

For the measurements without the grid, the results from station 1 (very close to the wing) give a better result than the other station. These results have been compared with the Lamb-Oseen model. The measurement result for station 1 is the closest one to the Lamb Oseen model, and it gives consistent results. It is challenging to analyze the result from the measurement with a turbulence grid. Because the result is inconsistent.

In this research, it is found that the circulation decreases in the downstream direction. In contradiction with the physics law, that the circulation should be constant for a confined isolated vortex. The measurement technique probably and the method of determining the circulation are probably the leading causes of this phenomenon. It is vital for future development; capturing vortex in the tunnel and determining the airflow circulation needs to be improved.

ACKNOWLEDGEMENT

The researcher is very grateful to , dr. M. Ren, ir. A.Elsenaar, dr. ir. R.R Trielling, prof. dr. ir. G.J.F van Heijst, prof.dr.ir. W. van de Water from Fluid Dynamics Laboratory Eindhoven University of Technology, for their major contribution to this project.

REFERENCES

1. Zhipeng L, Yuyun B, Zhengming G. PIV experiments and large eddy simulations of single-loop flow fields in Rushton turbine stirred tanks,. Chem Eng Sci. 2011;66(6):1219–31.
2. Crow S., Bate, E.R. J. Lifespan of trailing vortices in turbulent atmosphere. J Aircr. 1976;13(7):476–82.
3. NASA Dryden Flight Research Center. Wake Vortex Research. Technology Facts. 2004;1–6.
4. Technology E, Centre IC. International Conference of Mechanical Engineering, Energy Technology and Management, IMEETMCON 2018, September 4-7, 2018, International Conference Centre, University of Ibadan, Ibadan, Nigeria. 2018;43–50.
5. Kolář V. Vortex identification: new requirements and limitation. Int J Heat Fluid Flow. 2007;28:638–52.
6. Atoyebi M, Ismail O, Dare AA, Salau TAO. Lift Characterization Of An Airfoil Embedded. In: International Conference of Mechanical Engineering, Energy Technology and Management, IMEETMCON 2018. Ibadan: University of Ibadan, Nigeria; 2018.
7. Chakraborty P, Balachandar S, Adrian R. On the relationships between local vortex identification schemes. J Fluid Mech. 2005;535:189–214.
8. Gregorio F De, Visingardi A. Vortex detection criteria assessment for PIV data in rotorcraft applications. Exp Fluids. 2020;61:3012.
9. Liu C, Wang Y, Yang Y. New omega vortex identification method. Sci China Physics, Mech Astron. 2016;59(8):684711.
10. Liu HT. Effects of Ambient Turbulence on the Decay of a Trailing Vortex Wake. J Aircr. 1992;29(2):255–63.
11. Jeong J, Hussain F. On the identification of a vortex. J Fluid Mech. 1995;285:69–94.
12. Graftieaux L, Michard M, Grosjean N. Combining PIV, POD and vortex identification algorithms for the study of unsteady turbulent swirling flows. Meas Sci Technol. 2001;12(9):1422–9.
13. Ren M, Rindt CCM, Steenhoven AA Van. Experimental and numerical investigation of the vortex formation process behind a heated cylinder. Phys FLUIDS. 2004;16(8):3103–14.
14. van der Spek A. Linear and non-linear theories of flow through an actuator disk. Eindhoven University of Technology MASTER; 1986.
15. Vavilov VP, Lutsenko A V. Infrared Physics & Technology Evaluating characteristics of turbulent fl ames by using IR thermography and PIV. Infrared Phys Technol [Internet]. 2018;92(April):240–3. Available from: https://doi.org/10.1016/j.infrared.2018.06.006
16. Xiao J, Wu J, Chen L, Shi Z. Particle image velocimetry (PIV) measurements of tip vortex wake structure of wind turbine. Appl Math Mech. 2011;32:729–38.
17. Atkins MD. Velocity Field Measurement Using Particle Image Velocimetry (PIV). In: Tongbeum Kim, Tian Jian Lu SJS, editor. Application of Thermo-Fluidic Measurement Techniques [Internet]. Butterworth- Heinemann; 2016. p. 125–66. Available from: http://www.sciencedirect.com/science/article/pii/B9780128097311000058
18. Brossard C, Monnier JC, Barricau P, Vandernoot FX, Sant Y Le, Besnerais G Le, et al. Principles and applications of particle image velocimetry T. Aerosp LAB [Internet]. 2009;(1):1–11. Available from: https://hal.archives-ouvertes.fr/hal-01180587
19. Elsinga GE. Tomographic particle image velocimetry.
20. Ghimire HC. WING-TIP VORTEX EVOLUTION IN TURBULENCE. 2018;13023.
21. Mulleners K, Raffel M. The onset of dynamic stall revisited. Exp

Fluids. 2012;52(3):779–93.
22. Liu C, Gao Y, Tian S, Dong X. Rortex — a new vortex vector definition and vorticity tensor and vector decompositions. Phys Fluids. 2018;30:35103.
23. Westerweel J, Scarano F. Universal outlier detection for PIV data. Exp Fluids. 2005;39:1096–100.